The role of inertia in the rupture of ultrathin liquid films

Cite as: Phys. Fluids **32**, 112114 (2020); https://doi.org/10.1063/5.0031430
Submitted: 30 September 2020 . Accepted: 03 November 2020 . Published Online: 24 November 2020

D. Moreno-Boza, A. Martínez-Calvo, and A. Sevilla

Physics of Fluids ARTICLE scitation.org/journal/phf

The role of inertia in the rupture of ultrathin liquid films

Cite as: Phys. Fluids 32, 112114 (2020); doi: 10.1063/5.0031430
Submitted: 30 September 2020 • Accepted: 3 November 2020 •
Published Online: 24 November 2020

D. Moreno-Boza,[a] A. Martínez-Calvo,[b] and A. Sevilla[c]

AFFILIATIONS

Grupo de Mecánica de Fluidos, Departamento de Ingeniería Térmica y de Fluidos, Universidad Carlos III de Madrid, Av. Universidad 30, 28911 Leganés, Madrid, Spain

[a]**Author to whom correspondence should be addressed:** damoreno@pa.uc3m.es
[b]**Electronic mail:** amcalvo@ing.uc3m.es
[c]**Electronic mail:** asevilla@ing.uc3m.es

ABSTRACT

Theory and numerical simulations of the Navier–Stokes equations are used to unravel the influence of inertia on the dewetting dynamics of an ultrathin film of Newtonian liquid deposited on a solid substrate. A classification of the self-similar film thinning regimes at finite Ohnesorge numbers is provided, unifying previous findings. We reveal that, for Ohnesorge numbers smaller than one, the structure of the rupture singularity close to the molecular scales is controlled by a balance between liquid inertia and van der Waals forces, leading to a self-similar asymptotic regime with $h_{\min} \propto \tau^{2/5}$ as $\tau \to 0$, where $h_{\min}$ is the minimum film thickness and τ is the time remaining before rupture. The flow exhibits a three-region structure comprising an irrotational core delimited by a pair of boundary layers at the wall and at the free surface. A potential-flow description of the irrotational core is provided, which is matched with the vortical layers, allowing us to present a complete parameter-free asymptotic description of inertia-dominated film rupture.

I. INTRODUCTION

A growing number of emerging technologies involve the manipulation of liquid metals from millimeter to sub-micron scales.[7,8,15] For instance, in additive manufacturing and electronics, liquid gallium has received special attention mainly due to its non-toxic character and its low melting point, just slightly above room temperature. In addition, plasmonic devices and many patterning and coating processes rely on metal or metal-like materials such as silver and gold. Many of these applications involve the presence of liquid jets, liquid droplets, and thin liquid films in critical intermediate stages. In particular, thin liquid films have been extensively studied due to their central role in many engineering devices, as well as in geological and physiological flows (see Refs.4–6 and Ref. 20 for thorough and excellent reviews). In most of the previous theoretical studies of liquid film dynamics, the effect of liquid inertia has been neglected, an approximation that is highly accurate when the characteristic length scale is small and the liquid viscosity is large. In contrast, inertia cannot be neglected when the working fluid is a liquefied metal, as clearly pointed out in a number of recent investigations.[11,12,15,16,18]

In the present work, we report a theoretical and numerical study of the influence of liquid inertia on the instability, nonlinear dynamics, and rupture of ultra-thin liquid films placed on a solid impermeable substrate, which are known to become unstable in the non-wetting case due to the action of the long-range van der Waals (vdW) forces. In particular, we study and classify the self-similar regimes that are transiently achieved as gas–solid contact is approached, allowing us to provide a unified description of all previous theoretical findings. We also deduce a new non-slender inertial regime in which the minimum film thickness scales with the time to contact as $h_{\min} \propto \tau^{2/5}$, stemming from a balance between liquid inertia and vdW forces, the capillary force being asymptotically subdominant. The latter result complements the existing descriptions of the inertial limit, which predict $h_{\min} \propto \tau^{2/7}$ from a balance of liquid inertia with capillary and vdW forces,[10,25] in that the latter slender flow regimes experience a crossover to the newly found solution due to the breakdown of slenderness when the molecular scale is approached.

This paper is organized as follows: In Sec. II, we present the mathematical model used to describe the inertial dewetting flow, and we present numerical integrations of the Navier–Stokes equations

aimed at establishing its main dynamical features. In Sec. III, we first provide an exhaustive classification of the asymptotic self-similar regimes during film thinning at finite Ohnesorge numbers. We then focus on the inertial near-rupture flow in Sec. IV, including the universal self-similar potential flow in the bulk of the liquid film, as well as the wall and free-surface boundary layers. Some concluding remarks are finally presented in Sec. V.

II. GOVERNING EQUATIONS AND NUMERICAL RESULTS

A. Navier–Stokes equations

We consider the incompressible flow resulting from the thinning of a dewetting two-dimensional thin liquid film of density ρ, viscosity μ, and initial thickness h_o^*, initially resting on a solid substrate and separated from a passive immiscible ambient by an interface of constant surface tension coefficient σ. Such films are known to become unstable to infinitesimal perturbations due to long-range intermolecular forces when the film thickness lies below a thickness threshold of about the 100 nm.[3,23] The overall actions of such forces are modeled through a disjoining pressure term with the associated potential per unit volume $A/(6\pi h^3)$, where A is the Hamaker constant[13] reflecting the strength of the intermolecular interactions. Note that this potential is derived for the particular case of the vdW force between two parallel surfaces. Although the rigorous way to compute these long-range forces would imply the need to solve an integro-differential problem for the coupled evolution of these forces and the flow, the latter task has never been attempted to study thin-film rupture, at least as far as we know. The simplification used in all hydrodynamic studies consists in substituting the exact integral of the vdW potential, either by the parallel-plane approximation used in the present manuscript, in most cases, or by introducing corrections to the disjoining pressure that take into account non-parallelism.[1] It should be pointed out that the local flow in the immediate vicinity of the minimum interface radius could be very similar using the exact representation, since by definition, the local slope of the interface is zero at the minimum. However, the only way to check the latter hypothesis is performing an actual calculation of the full integro-differential description, a formidable task that we have not attempted. To describe the resulting unstable dynamics, we make use of the so-called *augmented* incompressible Navier–Stokes equations, which are non-dimensionalized upon taking

$$\ell_c = a = \sqrt{\frac{A}{6\pi\sigma}}, \quad v_c = \sqrt{\frac{A}{6\pi\rho a^3}}, \tag{1}$$

$$t_c = \frac{a}{v_c} = \sqrt{\frac{\rho a^3}{\sigma}}, \quad p_c = \phi_c = \frac{A}{6\pi a^3} \tag{2}$$

as the characteristic length, velocity, time, pressure, and intermolecular potential scales, respectively, where a is the molecular length scale and v_c is a characteristic velocity straightforwardly derived from a balance between liquid inertia and vdW forces (see Sec. III). Note also that t_c can be interpreted as the capillary time based on a. We would like to point out that the reason for our selection of a as the relevant length scale, instead of the more common choice of h_o^*, is due to the fact that, here, we focus on the film thinning dynamics near its rupture. Thus, we expect that the local flow close to the singularity loses memory of the initial conditions, and in particular, the initial thickness h_o^* should become irrelevant during the last stages. The use of the scales (1) yields

$$\nabla \cdot \boldsymbol{v} = 0, \quad \boldsymbol{x} \in \mathcal{V}, \tag{3a}$$

$$\frac{\mathrm{D}\boldsymbol{v}}{\mathrm{D}t} = -\nabla h^{-3} + \nabla \cdot \boldsymbol{T}, \quad \boldsymbol{x} \in \mathcal{V}, \tag{3b}$$

as the relevant equations of motion, where $\boldsymbol{T} = -p\boldsymbol{I} + Oh(\nabla \boldsymbol{v} + \nabla \boldsymbol{v}^{\mathrm{T}})$ is the stress tensor of the fluid, $\mathrm{D}/\mathrm{D}t = \partial_t + \boldsymbol{v} \cdot \nabla$ is the substantial derivative, $Oh = \mu/\sqrt{\rho a \sigma} = \mu[6\pi/(\rho^2 A\sigma)]^{1/4}$ is the Ohnesorge number based on a, $\mathcal{V}$ is the liquid film domain, $\boldsymbol{x} = (x, y)$ are Cartesian coordinates, and $\boldsymbol{v} = (u, v)$ is the velocity field, assumed to be two-dimensional. We note here that the first authors to include the disjoining pressure as an augmented pressure in the full Navier–Stokes equations were Ruckenstein and Jain,[22] followed later on by many investigators such as Oron *et al.*,[20] Craster and Matar,[5] and Blossey.[3] Note also that the exploring the equivalent axisymmetric configuration, leading to film breakup modes of hole or ring type,[25] is certainly interesting but is out of the scope of the present study. At the free surface $\partial\mathcal{V}$, we impose the kinematic and stress balance boundary conditions, which read

$$\boldsymbol{n} \cdot (\partial_t \boldsymbol{x}_s - \boldsymbol{v}) = 0, \quad \boldsymbol{x} \in \partial\mathcal{V}, \tag{4a}$$

$$\boldsymbol{T} \cdot \boldsymbol{n} = -\boldsymbol{n}(\nabla \cdot \boldsymbol{n}), \quad \boldsymbol{x} \in \partial\mathcal{V}, \tag{4b}$$

respectively, where $\boldsymbol{x}_s$ is the parameterization of the interface, located at $y = h(x, t)$, and $\boldsymbol{n}$ is the unit normal vector to the interface. At the solid substrate, $y = 0$, the no-slip and no-penetration boundary condition is enforced, $\boldsymbol{v} = \boldsymbol{0}$. As for the initial conditions, in the numerical simulations, we consider half wavelength of a spatially periodic liquid film, and thus, we impose the symmetry condition, that is, $u = 0$ and no shear stress $\boldsymbol{T} \cdot \boldsymbol{e}_x = \boldsymbol{0}$ at $x = 0$ and $x = \pi/k$, where $k < k_c = \sqrt{3}/h_o^2$ is the dimensionless wavenumber of the initially perturbed interface $\boldsymbol{x}_s = [x, h_o\,(1 - \varepsilon \cos kx)]$ imposed at $t = 0$. Here, k_c is the dimensionless cut-off wavenumber predicted by linear instability theory[23] (also Appendix A), $h_o = h_o^*/a$ is the initial film thickness normalized with the molecular length scale, and ε is a small positive constant that triggers the instability and induces the rupture of the liquid film at $x = 0$ and $t = t_{\mathrm{R}}$.

Two non-dimensional parameters govern the flow at hand, namely, the dimensionless initial film thickness, h_o, and the molecular Ohnesorge number, Oh. These two parameters can be written in terms of the Weber and Ohnesorge numbers defined when taking the global scales, thus the appropriate ones to describe the initial linear regime of the thinning. These are the same scales as in (1) but substitute a by h_o^* everywhere. In particular, the corresponding characteristic velocity v_{cl} is given by the balance $\rho v_{cl}^2/h_o^* \sim A/(6\pi h_o^{*4}) \Rightarrow v_{co}^2 = A/(6\pi\rho\sigma h_o^{*3})$ (see Appendix A). Using these global scales, the corresponding Weber and Ohnesorge numbers are $We = \rho v_{cl}^2 h_o^*/\sigma = h_o^{-2}$ and $Oh_l = Oh\sqrt{h_o} = OhWe^{-1/4}$. Note that none of these Ohnesorge numbers are the most commonly used, $Oh_o = \mu/\sqrt{\rho\sigma h_o^*} = Oh/\sqrt{h_o} = OhWe^{1/4}$, and thus $Oh = Oh_l Oh_o$, which, henceforth, will be called *global* Ohnesorge number.

B. Numerical simulations of the flow evolution toward the singularity

The finite-element method recently employed by Ref. 19 was slightly modified to integrate (3) and (4) for a wide range of values of Oh and h_o. More details about the numerical method can be found in Appendix C. As the film evolved toward rupture, we tracked the minimum film thickness $h_{\min} = h(0, t)$, the maximum streamwise velocity, $u_{\max}$, and the maximum wall shear stress, $\tau_{xy} = \partial_y u|_{y=0}$. Note that the existence of a power law $h_{\min} \propto \tau^n$ for some value of $n > 0$, where $\tau = t_R - t$ is the time remaining to rupture, is a local self-similarity test that can be easily extracted from the numerical simulations. Figure 1 shows several representative film evolutions revealing that $(h_{\min}, u_{\max}, \tau_{xy}) \propto (\tau^{2/5}, \tau^{-3/5}, \tau^{-11/10})$ as $\tau \to 0$ for all the values of h_o and sufficiently small values of Oh. However, it is important to emphasize that the latter universal behavior is achieved for $(\tau, h_{\min}) \lesssim (0.01, 0.16)$, for which the continuum approximation is compromised. We thus conclude that the 2/5 power law would never be fully established under realistic conditions. For $\tau \gtrsim 0.01$ and $h_o \lesssim 30$, the results of Fig. 1 show no sign of sustained power-law behavior for $Oh \lesssim 1$, as revealed by the instantaneous exponents $n(\tau) = \mathrm{d}\log_{10} h_{\min}/\mathrm{d}\log_{10}\tau$ plotted in Figs. 1(b) and 1(c).

In particular, Fig. 1(b) reveals that, for all the cases where $Oh \ll 1$, the value of n increases monotonically with $n(\tau) \to 2/5$ as $\tau \to 0$ independently of h_o. It is also deduced that the function $n(\tau)$ has no inflection points for the smallest values of h_o, namely, $h_o = 1$ and $h_o = 3.16$, indicating the absence of intermediate self-similarity other than the 2/5 power law, which, as shown in Sec. III, is due to a balance between liquid inertia and vdW forces with negligible surface tension and viscous forces (regime IV of Table I). However, for

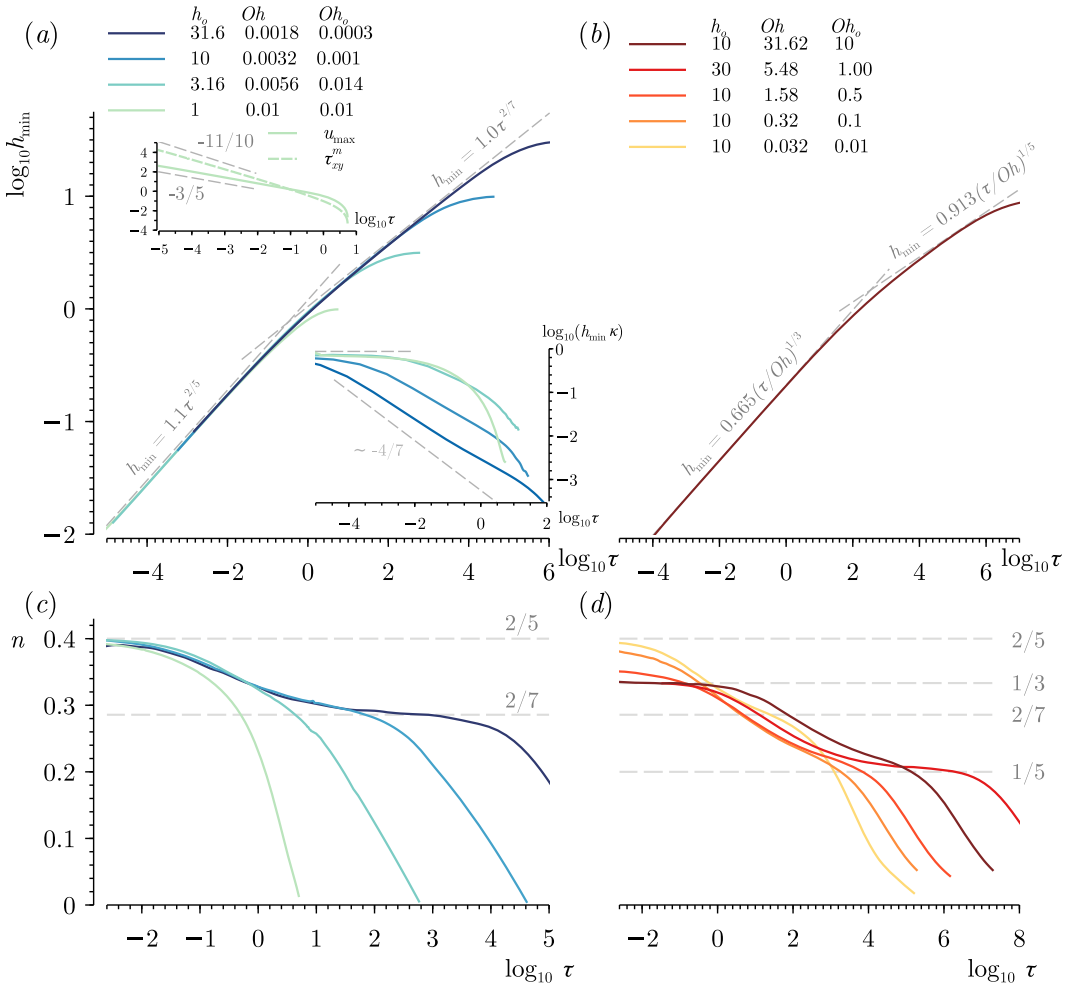

FIG. 1. (a)–(b) The function $\log_{10} h_{\min}(\log_{10}\tau)$ for different values of h_o and Oh indicated in the legend. The gray dashed lines show the self-similar thinning laws associated with regimes I–IV in Table I. The top inset displays the maximum streamwise velocity, $u_{\max}$, and the maximum shear stress at the wall τ_{xy}^m for $h_o = 1$ and $Oh = 10^{-2}$. The bottom inset shows the curvature at the minimum normalized with the minimum thickness, $h_{\min}\kappa$, for the different cases indicated in the legend (solid lines), together with the scaling law $h_{\min}\kappa \propto \tau^{-4/7}$ (dashed line), deduced from the scales of regime III.[10] The instantaneous exponent $n(\tau)$: (c)–(d) influence of h_o for $Oh \ll 1$ and influence of Oh for $h_o = (10, 30)$.

TABLE I. The four thinning regimes during the rupture of ultrathin liquid films. In the balances, ρ, μ, and σ stand for the liquid inertia, the viscous forces, and the capillary forces, respectively. The references stand for Zhang and Lister[25] (ZL99), Moreno-Boza *et al.*[19] (MB20), and Garg *et al.*[10] (GA17).

Regime	Validity	Balance	Realisability	$h_{\min}(\tau)$	$\kappa(\tau)h_{\min}(\tau)$	References
I	$\varepsilon_l Re_l \ll 1, \varepsilon_l \ll 1$	vdW-μ-σ	$Oh \gtrsim h_o^{-3/2}$	$(\tau/Oh)^{1/5}$	$(\tau/Oh)^{-2/5}$	ZL99
II	$\varepsilon_l Re_l \ll 1, \varepsilon_l \sim 1$	vdW-μ	$Oh \gtrsim h_o^{-3/2}$	$(\tau/Oh)^{1/3}$	~ 1	MB20
III	$\varepsilon_l Re_l \gg 1, \varepsilon_l \ll 1$	vdW-ρ-σ	$Oh \lesssim 1$	$\tau^{2/7}$	$\tau^{-4/7}$	GA17
IV	$\varepsilon_l Re_l \gg 1, \varepsilon_l \sim 1$	vdW-ρ	$Oh \lesssim 1$	$\tau^{2/5}$	~ 1	Present work

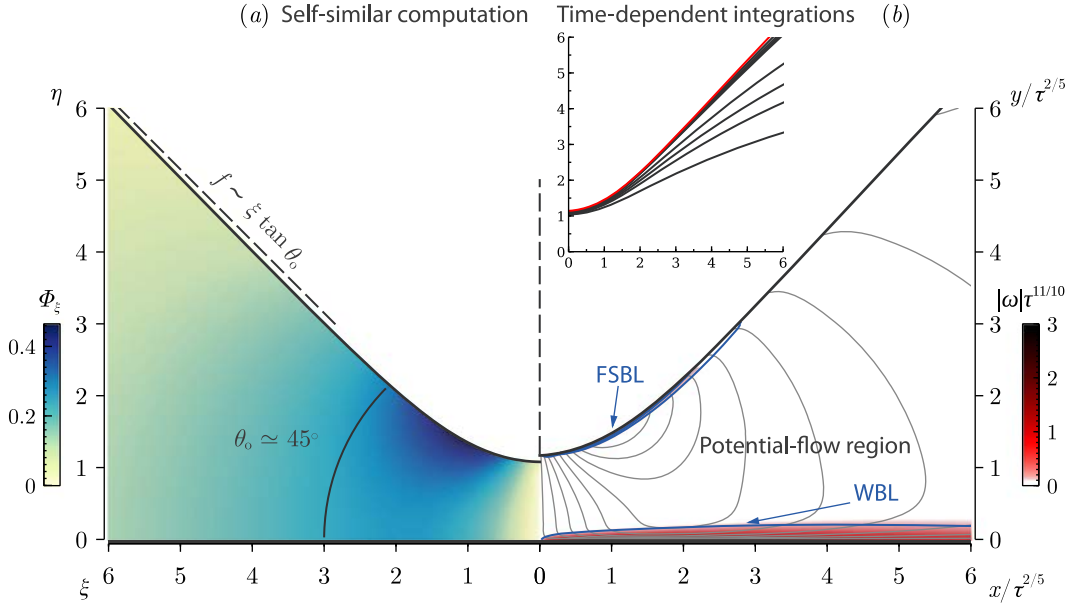

FIG. 2. (a) Contours of longitudinal velocity, $\Phi_\xi(\xi, \eta)$, obtained from the self-similar potential flow. The free surface is wedge-shaped, with an angle θ_o = 45° off the solid wall. (b) Snapshot of a numerical simulation performed for Oh = 0.01 and h_o = 1 at $\tau = 4.41 \times 10^{-6}$, with ε = 0.01 and $k = 0.3k_c$. Solid lines represent contours of longitudinal velocity, and colors represent contours of normalized vorticity, $|\omega|\tau^{11/10}$. The inset shows instantaneous re-scaled film shapes for $\tau = (0.027, 6.98 \times 10^{-3}, 2.98 \times 10^{-3}, 9.81 \times 10^{-4}, 8.13 \times 10^{-5}, 6.13 \times 10^{-5}, 4.13 \times 10^{-5}, 2.13 \times 10^{-5}, 4.41 \times 10^{-6})$ illustrating the self-similar collapse.

h_o = 10 and h_o = 31.6, an inflection point appears in the evolution of $n(\tau)$ near the value n = 2/7, which corresponds to the regime described by Garg *et al.*[10] as a local balance between liquid inertia, vdW forces, and surface tension forces (regime III of Table I). Although for $h_o \leq 31.6$, the 2/7-regime is only established for less than a decade, its range of validity increases with increasing h_o. Indeed, Garg *et al.*[10] reported Navier–Stokes simulations for h_o = 1165, the case in which the 2/7 regime is established for several decades for a shear-thinning liquid.

The effect of liquid viscosity on the rupture regimes is deduced from Fig. 1(c), where $n(\tau)$ is plotted for several values of Oh and h_o = (10, 30). As the value of Oh increases, the film is seen to pass through a number of intermediate self-similar regimes described in previous studies, although none of them are clearly established except in the limit $\tau \to 0$. As τ decreases, the 1/5 power law described by Zhang and Lister[25] (regime I of Table I) is first observed during a brief transient, followed by the 2/7-law for small enough values of Oh. For smaller values of τ, the 1/3-law described by Moreno-Boza *et al.*[19] (regime II in Table I) is clearly observed, holding until the singularity for Oh = 31.62. Finally, regime IV is reached as $\tau \to 0$ for $Oh \lesssim 1$.

As shown in Fig. 2(a) for $Oh = 10^{-2}$ and h_o = 1, the local rupture flow presents a distinctive multi-scale structure. The vorticity concentrates in boundary layers at the wall and at the free surface, surrounding a central irrotational core. The self-similar potential flow and the relevant scalings of the boundary layers are described in Sec. IV.

III. THE FILM THINNING REGIMES AT FINITE OHNESORGE NUMBERS

The results of Fig. 1 reveal the existence of different regimes during the thinning of the liquid film for finite values of Oh, which will now be explained using order-of-magnitude estimations of the

governing equations (3) and (4). Hereinafter, the dimensional variables with a non-dimensional counterpart will be denoted with an asterisk. We begin by defining two key variables, namely, the local slenderness and the local reduced Reynolds number,

$$\varepsilon_l(\tau_*) = \frac{h^*_{\min}}{x^*_c}, \tag{5a}$$

$$\varepsilon_l Re_l(\tau_*) = \frac{\rho u^*_c h^{*2}_{\min}}{\mu x^*_c} \sim \frac{\rho v^*_c h^*_{\min}}{\mu} \sim \frac{\rho h^{*2}_{\min}}{\mu \tau_*}, \tag{5b}$$

respectively, where $x^*_c(\tau_*)$ and $u^*_c(\tau_*)$ are the characteristic longitudinal length scale and velocity, respectively. Note that, in the last two estimations of Eq. (5b), the continuity Eq. (3a) has been used, providing the estimate $v^*_c \sim u^*_c \varepsilon_l$, where $v^*_c \sim h^*_{\min}/\tau_*$ is the characteristic transverse velocity. Note also that the local curvature at the minimum film thickness, $\kappa^* = \partial^2 h^*/\partial x^{*2}|_{x^*=0}$, can be estimated as

$$\kappa^*(\tau_*) \sim \frac{h^*_{\min}}{x^{*2}_c} \Rightarrow \kappa^* h^*_{\min} \sim \varepsilon_l^2, \tag{6}$$

and thus, the local curvature, measured with the instantaneous film thickness, is just the square of the slenderness parameter.

The momentum Eq. (3b) admits two limiting dominant balances depending on the value of $\varepsilon_l Re_l$, namely, the vdW–viscous balance when $\varepsilon_l Re_l \ll 1$ and the vdW–inertia balance when $\varepsilon_l Re_l \gg 1$. These two limiting cases will be explained in Subsections III A–III D.

A. Regimes under dominant viscous forces

The viscous regime prevails when $\epsilon_l Re_l \ll 1$, leading to the vdW–viscous balance

$$\frac{A}{h^{*3}_{\min} x^*_c} \sim \frac{\mu u^*_c}{h^{*2}_{\min}} \sim \frac{\mu v^*_c x^*_c}{h^{*3}_{\min}} \Rightarrow x^*_c \sim \left(\frac{A}{\mu}\right)^{1/2} \left(\frac{\tau_*}{h^*_{\min}}\right)^{1/2}, \tag{7}$$

with an associated local slenderness

$$\varepsilon_l \sim \left(\frac{\mu}{A}\right)^{1/2} \frac{h^{*3/2}_{\min}}{\tau_*^{1/2}}. \tag{8}$$

Assuming the similarity ansatz $h^*_{\min} \propto \tau_*^{\alpha}$, it is deduced that

$$\varepsilon_l \propto \tau_*^{(3\alpha-1)/2} \tag{9}$$

so that asymptotic slenderness as $\tau \to 0$ requires that $\alpha > 1/3$. Two different values of α leading to self-similar regimes are possible depending on the value of ε_l, as described in Secs. III A 1 and III A 2.

1. The slender viscous regime

When $\epsilon_l \ll 1$, the local flow is slender, $x^*_c \gg h^*_{\min}$, and thus, the capillary pressure gradient is written as

$$\sigma \frac{\partial \kappa^*}{\partial x^*} \sim \sigma \frac{h^*_{\min}}{x^{*3}_c}, \tag{10}$$

and its relative importance over the driving vdW force is $O[(\sigma/A) h^{*4}_{\min}/x^{*2}_c] \sim (\mu\sigma/A^2) h^{*5}_{\min}/\tau_* \propto \tau_*^{5\alpha-1}$, implying that $\alpha \geq 1/5$. Note that vdW, viscous, and surface tension forces are in balance when $\alpha = 1/5$, leading to the rupture law

$$h^*_{\min} \sim \left(\frac{A^2}{\mu\sigma}\right)^{1/5} \tau_*^{1/5}, \tag{11}$$

discovered by Zhang and Lister.[25] In the latter regime, which is referred to as *Regime I* in Table I, the local slenderness and the local Reynolds number scale correspondingly as

$$\varepsilon_l \sim \left(\frac{\mu^2 A}{\sigma^3}\right)^{1/5} \tau_*^{-2/5}, \tag{12a}$$

$$\varepsilon_l Re_l \sim \frac{\rho A^{4/5}}{\mu^{7/5}\sigma^{2/5}} \tau_*^{-3/5}. \tag{12b}$$

2. The non-slender viscous regime

The self-similar solution (11) fails when $\epsilon_l \sim 1$ due to the breakdown of slenderness.[25] The latter condition holds at the crossover time,

$$\tau_* = \tau_{*\varepsilon} \sim \frac{\mu A^{1/2}}{\sigma^{3/2}}, \tag{13}$$

with the associated minimum thickness

$$h^*_{\min}(\tau_{*\varepsilon}) \sim \left(\frac{A}{\sigma}\right)^{1/2} \sim a \Rightarrow h_{\min}(\tau_\varepsilon) \sim 1. \tag{14}$$

Equation (14) implies a breakdown of the 1/5 power law close to the molecular scale, as studied in detail by Moreno-Boza *et al.*[19] Indeed, note that the breakdown of slenderness that occurs when $\varepsilon_l \sim 1$ gives rise to a regime given by the balance $A/(h^{*4}_{\min}) \sim \mu u^*_c/h^{*2}_{\min} \sim \mu/(h^*_{\min}\tau_*)$, yielding the asymptotic thinning law

$$h^*_{\min} \sim \left(\frac{A}{\mu}\right)^{1/3} \tau_*^{1/3}, \tag{15}$$

discovered by Moreno-Boza *et al.*[19] where a detailed description is given in their work.

B. The viscous–inertial crossover

Apart from the breakdown of slenderness described in Sec. III A 2, the self-similar solution (11) may also fail when $\varepsilon_l Re_l \sim 1$ due to the onset of inertial effects at a crossover time given by

$$\tau_* = \tau_{*\rho} \sim \frac{\rho^{5/3} A^{4/3}}{\mu^{7/3}\sigma^{2/3}}, \tag{16}$$

with the associated minimum thickness

$$h^*_{\min}(\tau_{*\rho}) \sim \frac{\rho^{1/3} A^{2/3}}{\mu^{2/3}\sigma^{1/3}} \Rightarrow h_{\min}(\tau_\rho) \sim Oh^{-2/3}. \tag{17}$$

Equation (17) determines an inertial crossover at a length scale that depends on Oh with two relevant limiting cases. When $h_{\min}(\tau_\rho) \gtrsim h_o \Rightarrow Oh \lesssim h_o^{-3/2}$, liquid inertia is important from the onset film thinning, the case in which the 1/5 power law (11) is never established. On the other hand, when $h_{\min}(\tau_\rho) \lesssim 1 \Rightarrow Oh \gtrsim 1$, liquid inertia

becomes important at molecular scales, and the 1/5-law holds until $h_{\min} \sim 1$, when slenderness breaks down and Eq. (15) holds. In the intermediate case $h_o^{-3/2} \lesssim Oh \lesssim 1$, the 1/5 law experiences the inertial crossover at $h_{\min} \sim Oh^{-2/3}$.

C. Regimes under dominant inertia

As happened in the viscous case, the possible self-similar inertial regimes that are established when $\epsilon_l Re_l \gg 1$ depend on the local slenderness. Let us now describe the two corresponding limiting cases separately.

1. The slender inertial regime

We consider first the case with $\epsilon_l \ll 1$ for which the balance of liquid inertia and vdW forces yields

$$\rho u_c^{*2} \sim \frac{A}{h_{\min}^{*3}} \Rightarrow h_{\min}^{*3} x_c^{*2} \sim \frac{A}{\rho} \tau_*^2. \tag{18}$$

The ratio between the capillary pressure gradient, $O(\sigma h_{\min}^*/x_c^{*3})$, and the inertial force, $O(\rho u_c^{*2})$, is $O[(\rho\sigma/A^2) h_{\min}^{*7} \tau_*^{-2}] \propto (\rho\sigma/A^2)\tau_*^{7\alpha-2}$, implying that $\alpha \geq 2/7$. The case with $\alpha = 2/7$ corresponds to a balance of liquid inertia with vdW and surface tension forces and leads to the thinning law

$$h_{\min}^* \sim \left(\frac{A^2}{\rho\sigma}\right)^{1/7} \tau_*^{2/7}, \tag{19}$$

discovered by Garg *et al.*[10] in their analysis of shear-thinning liquids undergoing vdW-induced rupture. During this regime, the slenderness parameter is

$$\epsilon_l \sim \frac{\rho^{1/7} A^{3/14}}{\sigma^{5/14}} \tau_*^{-2/7} \tag{20}$$

so that the long-wave approximation breaks down when

$$\tau_* = \tau_{*\varepsilon} \sim \frac{\rho^{1/2} A^{3/4}}{\sigma^{5/4}} \Rightarrow h_{\min}^*(\tau_{*\varepsilon}) \sim \left(\frac{A}{\sigma}\right)^{1/2} \sim a, \tag{21}$$

implying that the slender inertial self-similar regime described by Eq. (19) fails when the molecular scales are approached, as happened in the viscous case explained in Sec. III A 2.

2. The non-slender inertial regime

As occurs in the viscous case, the slender inertial regime crosses over to a non-slender inertial regime when the molecular scales are approached, namely, $h_{\min} \sim 1$, the case in which the inertia–vdW balance transforms into $\rho h_{\min}^{*2}/\tau_*^2 \sim A/h_{\min}^{*3}$, leading to the asymptotic thinning law

$$h_{\min}^* \sim \left(\frac{A}{\rho}\right)^{1/5} \tau_*^{2/5}, \tag{22}$$

described here for the first time. It is interesting to note that a straightforward application of dimensional analysis naturally leads to Eq. (22) as a self-similar solution of the first kind for the vdW–Navier–Stokes system (see Appendix B). Finally, in the latter regime, the relative importance of the capillary pressure gradient compared with liquid inertia is $[\sigma^{10/7}/(\rho^{4/7}A^{6/7})]\tau_*^{8/7} \to 0$ as $\tau_* \to 0$ so that the ultimate regime reached just prior to rupture is a consistent dominant balance between inertia and vdW forces with asymptotically negligible surface tension forces.

D. Classification of the self-similar film thinning regimes

The previous development demonstrates the existence of four possible self-similar regimes during the vdW-induced rupture of the film at finite values of Oh, which are summarized in Table I. In dimensionless terms, these regimes are as follows: (I) When $\epsilon_l Re_l \ll 1$ and $\epsilon_l \ll 1$, the slender viscous regime discovered by Zhang and Lister[25] holds, with a minimum thickness $h_{\min} \sim (\tau/Oh)^{1/5}$ and a local curvature $\kappa \sim (\tau/Oh)^{-3/5}$. (II) When $\epsilon_l Re_l \ll 1$ and $\epsilon_l \sim 1$, the non-slender Stokes flow described by Moreno-Boza *et al.*[19] takes place, with $h_{\min} \sim (\tau/Oh)^{1/3}$ and $\kappa \sim h_{\min}^{-1}$. (III) When $\epsilon_l Re_l \gg 1$ and $\epsilon_l \ll 1$, the slender inertial regime reported by Garg *et al.*[10] prevails, with $h_{\min} \sim \tau^{2/7}$ and $\kappa \sim \tau^{-6/7}$. (IV) Finally, when $\epsilon_l Re_l \gg 1$ and $\epsilon_l \sim 1$, an ultimate non-slender inertial regime takes over, with $h_{\min} \sim \tau^{2/5}$ and $\kappa \sim h_{\min}^{-1}$. Since the latter regime is reported for the first time in the present paper, Sec. IV will be devoted to a detailed analysis of its main features.

Finally, let us provide a simple argument for the asymptotic sub-dominance of surface tension forces in the non-slender regimes II and IV. The intuition behind the latter fact is simply that, in these regimes, there is only one characteristic length scale, namely, $x_c^* \sim y_c^* \sim h_{\min}^*$. Thus, the local curvature $\kappa^* \sim (h_{\min}^*)^{-1} \to \infty$ as $\tau_* \to 0$, which diverges as the singularity is approached. What remains finite, however, is the local curvature scaled with the instantaneous minimum thickness, i.e., $\kappa^* h_{\min}^* \sim 1$ as $\tau_* \to 0$, explaining the fact that, in regimes II and IV, the shape of the interface is self-similar when appropriate variables are used to describe the local flow. Although surface tension forces diverge as $(h_{\min}^*)^{-2}$ toward the singularity, their sub-dominance is simply explained by the fact that vdW forces diverge as $(h_{\min}^*)^{-4}$ as $\tau_* \to 0$ and thus become much larger than surface tension forces in the last stages of the collapse close to the continuum limit.

IV. THE UNIVERSAL SELF-SIMILAR INERTIAL REGIME

Suggested by the flow evolution shown in Fig. 1 and by the order-of-magnitude analysis presented in Sec. III, the universal behavior $h_{\min} = 1.1\ \tau^{2/5}$ associated with regime IV in Table I will now be unveiled using similarity theory.

A. The self-similar potential flow

Letting $x = \tau^\beta \xi$, $y = \tau^\alpha \eta$, $u = \tau^\gamma U$, $v = \tau^{\gamma+\alpha-\beta} V$, $p = \tau^{-3\alpha} P$, and $h = \tau^\alpha f(\xi)$, where α, β, and γ are real numbers, a consistent leading-order dominant balance between inertia and vdW forces can indeed be found by substituting the similarity test into (3) and (4) and performing the limit $\tau \to 0$, yielding the exponents $\alpha = \beta = 2/5$ and $\gamma = \beta - 1 = -3/5$, in agreement with the results of Sec. III. To unravel the structure of the leading-order potential flow as $\tau \to 0$, we make use of the velocity potential Φ such that $U = \Phi_\xi$ and $V = \Phi_\eta$, reducing the description to the integration of the Laplace equation,

$$\Phi_{\xi\xi} + \Phi_{\eta\eta} = 0, \tag{23}$$

in $0 < \xi < \infty$ and $0 < \eta < f(\xi)$, where $f(\xi)$ is the *a priori* unknown shape of the free surface. Note that our strategy to unravel the non-slender inertial regime resembles that employed by Moreno-Boza

et al.[19] in the viscous case, where the biharmonic equation substitutes the Laplace equation. Hereinafter, subscripts denote partial derivatives unless stated otherwise. The leading-order contribution of the stress balance at the interface reduces to an Euler–Bernoulli-like boundary condition to be imposed together with the kinematic condition,

$$\frac{1}{f^3} + \frac{1}{5}\Phi + \frac{2}{5}(\xi\Phi_\xi + \eta\Phi_\eta) + \frac{1}{2}\left(\Phi_\xi^2 + \Phi_\eta^2\right) = 0, \tag{24a}$$

$$\frac{2}{5}f + \Phi_\eta - f_\xi\left(\frac{2}{5}\xi + \Phi_\xi\right) = 0, \tag{24b}$$

along $\eta = f$, together with the no-penetration condition $\boldsymbol{n}\cdot\nabla\Phi = 0$ at $\eta = 0$ and $\xi = 0$, where the gradient operator is applied with respect to ξ and η. The far-field boundary condition at $\xi \gg 1$ and $0 < \eta < f$ would require uniform matching with the inner flow solution for $x/\tau^{2/5} \ll 1$ and therefore is replaced by (24a) with the Hamaker term, i.e., $1/f^3$, switched off, which may alternatively be interpreted as a zero-pressure boundary condition. This enables us to give a fairly reasonable approximation to the real flow that is to be expected in the vicinity of the singularity. Problems of similar mathematical nature were derived, for instance, by Ref. 24 in the context of jets emerging from Faraday waves and by Ref. 19 to describe the self-similar Stokes flow leading to thin-film rupture for $Oh \gtrsim 1$. Equations (23)–(24b) were integrated using an algorithm similar to that described in Ref. 19, providing the free surface as part of the solution. A more comprehensive description of the numerical techniques employed to solve the problem is detailed in Appendix C.

The solution, shown in Fig. 2, exhibits a wedge-shaped film $f \sim (\xi - \xi_o)\tan\theta_o$ for some value of ξ_o, as $r \to \infty$ characterized by an opening angle $\theta_o \simeq 45°$ off the substrate, where $r^2 = (\xi - \xi_o)^2 + \eta^2$ and $\theta = \arctan\eta/\xi$ are polar coordinates. Examination of the far-field revealed that $\xi_o \simeq 0$ and $f(0) \simeq 1.08$. Also, a consistent radial decay of the potential of the form $\Phi \sim r^{-\lambda}$ along the ray $\theta = \theta_o$ was observed. The value of λ was seen to adjust quite well to 1/2 from the numerical computation [see the inset of Fig. 3(a)]. This is indeed the only value of λ that ensures compatibility in terms of powers of r in (24a). A noteworthy aspect of the result shown in Fig. 2 is the displacement effect of the wall boundary layer on the outer irrotational core. Indeed, the Navier–Stokes solution of Fig. 2(b) is seen to be slightly displaced in the positive y-direction with respect to the potential flow of Fig. 2(a).

The non-slender universal regime described in the present section is the inertial counterpart of the self-similar Stokes flow reported by Moreno-Boza *et al.*,[19] classified as regimes IV and II in Table I. It is noteworthy that the local interface shape in the Stokes case is also a wedge, but with an opening angle of 37° instead of the larger angle of 45° associated with inertial breakup.

B. The boundary layers

The potential solution described in Sec. IV A constitutes the outer flow for two vortical boundary layers sitting at the wall and at the free surface, briefly described in Secs. IV B 1 and IV B 2.

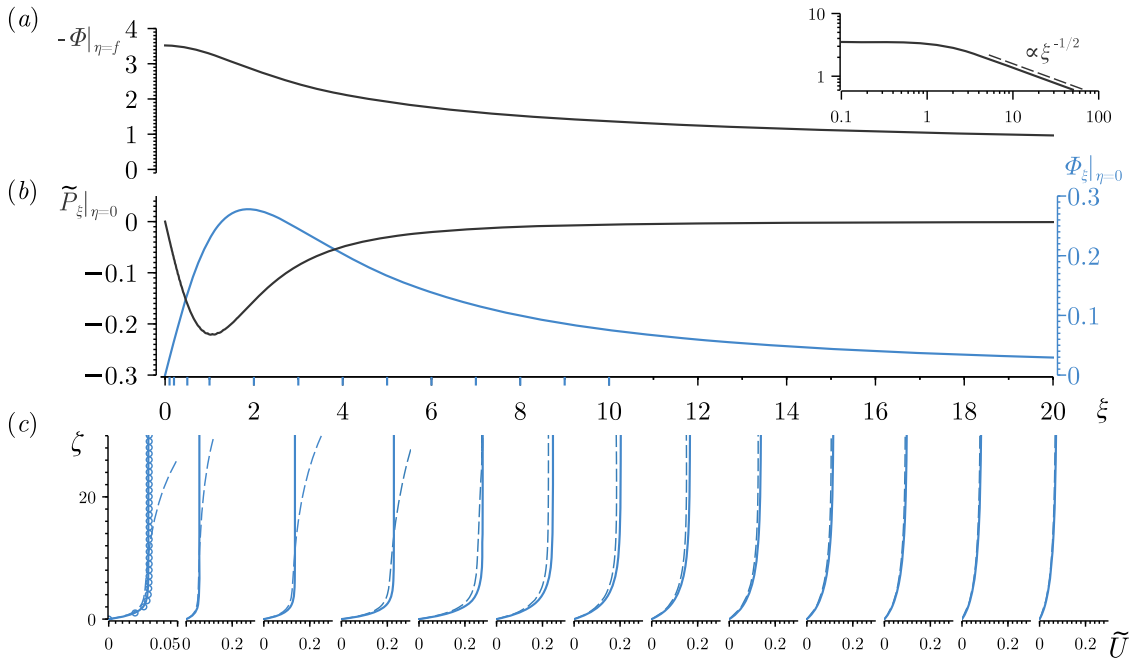

FIG. 3. (a) Velocity potential at the free surface (solid line) and its asymptotic behavior $-\Phi|_{\eta=f} \to \xi^{-1/2}$ for $\xi \gg 1$ (inset). (b) Wall slip velocity, $\Phi_\xi|_{\eta=0}$ (right axis), and wall pressure gradient, $P_\xi|_{\eta=0}$ (left axis). (c) Wall-boundary-layer velocity profiles at ξ = (0.1, 0.2, 0.5, 1, . . ., 10) (solid lines) and self-similar profile $\xi G'(\eta)$ at $\xi = 0.1$ (○). Accompanying numerical computations for $Oh = 0.01$, $h_o = 1$, and $\tau = 2.13 \times 10^{-5}$ (data from Fig. 2) are also shown to illustrate agreement (dashed lines).

1. The wall boundary layer

The slipping velocity at the wall $\Phi_\xi|_{\eta=0}$ and the streamwise pressure gradient $P_\xi|_{\eta=0}$, evaluated numerically and presented in Fig. 3(b), serve as boundary conditions for the viscous wall boundary layer (WBL). The thickness of the WBL, δ_w^*, is given by the balance $\rho u_c^{*2}/x_c^* \sim \mu u_c^*/\delta_w^{*2}$, whence

$$\delta_w^* \sim \frac{\mu \tau_*}{\rho} \Rightarrow \delta_w \sim Oh^{1/2}\tau^{1/2}. \tag{25}$$

The wall shear stress (WSS) $\tau_{xy}^* \sim \mu u_c^*/\delta_w^*$, yielding

$$\tau_{xy}^* \sim \frac{\mu^{1/2}\sigma^{11/8}}{\rho^{1/4}A^{5/8}}\tau_*^{-11/10} \Rightarrow \tau_{xy} \sim Oh^{-1/2}\tau^{-11/10}, \tag{26}$$

as confirmed by the evolution of the shear stress in Fig. 1.

The substitution into (3) of the standard boundary-layer change in variables,[21] namely,

$$\begin{aligned} x &= \tau^{2/5}\xi, \quad y = (Oh\tau)^{1/2}\zeta, \\ u &= \tau^{-3/5}\tilde{U}, \quad v = (Oh/\tau)^{1/2}\tilde{V}, \\ p &= \tau^{-6/5}\tilde{P}, \quad h = (Oh\tau)^{-1/2}\tilde{h}(\xi), \end{aligned} \tag{27}$$

yields the leading-order problem

$$\tilde{U}_\xi + \tilde{V}_\zeta = 0, \tag{28a}$$

$$\frac{3}{5}\tilde{U} + \left(\frac{2\xi}{5} + \tilde{U}\right)\tilde{U}_\xi + \left(\frac{\zeta}{2} + \tilde{V}\right)\tilde{U}_\zeta = -\tilde{P}_\xi + \tilde{U}_{\zeta\zeta}, \tag{28b}$$

$$\tilde{P}_\zeta = 0, \tag{28c}$$

describing the WBL so that the pressure gradient is given by the external potential flow as $-\tilde{P}_\xi = [(\Phi_\xi + 2\xi/5)\Phi_{\xi\xi} + 3\Phi_\xi/5]|_{\eta=0}$. The boundary conditions accompanying the system (28) are $\tilde{U} = \tilde{V} = 0$ at $\zeta = 0$, $\tilde{U} \to \Phi_\xi$ as $\zeta \to \infty$, and $\tilde{U} = 0$ at $\xi = 0$. The parabolic system (28) is integrated using the method of lines, whose details are described in Appendix C. To obtain the initial condition, we take advantage of the self-similar nature of the boundary layer for $\xi \ll 1$. Indeed, the substitution of a stream function $\xi G(\zeta)$ into (28a) and (28b) yields

$$G''' + (G - \zeta/2)G'' - G'(G' + 1) = \xi^{-1}\tilde{P}_\xi, \tag{29}$$

with the boundary conditions $G = G' = 0$ at $\zeta = 0$ and $G' \to \xi^{-1}\Phi_\xi$ as $\zeta \to \infty$. Equation (29) admits a self-similar solution for $\xi \ll 1$ in which $\xi^{-1}\tilde{P}_\xi \to -0.3802$ and $\xi^{-1}\Phi_\xi \to 0.2965$, which was computed using a pseudospectral collocation technique.[9]

2. The free-surface boundary layer

Finally, for conciseness, let us just provide the characteristic scales of the free-surface boundary layer (FSBL). Its thickness, δ_f^* can be estimated by taking into account that the free-surface vorticity is $\omega_f^* = -2\partial_s v_s^* + 2u_s^*\kappa^*$ in a two-dimensional unsteady flow,[17] where ∂_s is the derivative along the interface, u_s^* and v_s^* are the tangential and normal velocity components at the interface, and κ^* is the twice the mean curvature. We now take into account that, in regime IV, $u_s^* \sim v_s^* \sim u_c^* \sim h_{\min}^*/\tau_*$ and $\partial_s \sim \kappa^* \sim 1/a$, providing $\omega_f^* \sim h_{\min}^*/(a\tau_*)$. Since, by definition, the vorticity is $\omega_f^* \sim \Delta u_s^*/\delta_f^*$, we deduce that $\delta_f^* \sim a\tau_*\Delta u_s^*/h_{\min}^*$, where Δu_s^* is the characteristic velocity increment across the FSBL. In turn, the value of Δu_s^* may be estimated by balancing the convective acceleration with the capillary pressure gradient, $\rho u_c^*\Delta u_s^*/\Delta x^* \sim \sigma\kappa^*/\Delta x^* \Rightarrow \Delta u_s^* \sim \sigma/(\rho a u_c^*)$. Thus, we deduce that $\delta_f^* \sim \sigma/(\rho u_c^{*2})$, finally yielding

$$\delta_f^* \sim \frac{\sigma}{\rho^{3/5}A^{2/5}}\tau_*^{6/5} \Rightarrow \delta_f \sim \tau^{6/5}, \tag{30}$$

for the FSBL thickness that, as deduced from Eq. (30), does not depend on Oh in contrast with the WBL thickness (25). We finally note that $\delta_f \to 0$ as $\tau \to 0$ much faster than the WBL, in agreement with the results shown in Fig. 2.

V. CONCLUDING REMARKS

New insights into the inertia-driven dewetting of unstable ultrathin films of Newtonian liquids have been gained through theoretical analysis and numerical integration of the Navier–Stokes equations. We have shown that when the Ohnesorge number $Oh \lesssim 1$, the final approach of the flow toward the rupture singularity close to the molecular scales is self-similar, with a non-dimensional minimum film thickness $h_{\min} = 1.1\,\tau^{2/5}$ due to a dominant balance between liquid inertia and van der Waals forces, with asymptotically subdominant surface tension forces. The spatial structure of the flow in this new regime presents a distinguished three-region structure characterized by a potential core separated by two boundary layers, namely, a vortical curvature-induced layer sitting at the free surface and a viscous layer adhered to the solid substrate. It is interesting to note that when $Oh \ll 1$, the latter three-region structure is already present from the onset of the vdW-induced instability, as demonstrated in Appendix A by making use of linearized theory. Upon introducing appropriate self-similar variables, the irrotational core has been described as a universal solution to the Euler equations, featuring a wedge-shaped interface with an opening angle of 45° off the solid. The latter non-slender solution applies when the minimum film thickness approaches the molecular scale, as obtained similarly by Moreno-Boza *et al.*[19] in the context of viscous dewetting. A parameter-free description of the viscous wall layer of non-dimensional thickness $\delta_w \sim Oh^{1/2}\tau^{1/2}$ has been provided by integrating Prandtl's equations using self-similar boundary-layer variables. We have also explained why the free-surface vortical layer is much thinner than the viscous wall layer, since its thickness scales as $\delta_f \sim \tau^{6/5} \ll \delta_w$ as $\tau \to 0$.

For finite values of the Ohnesorge number, an order-of-magnitude analysis allowed us to classify all the possible regimes of dewetting of Newtonian liquids, thereby unifying previous studies. The slender viscous regime discovered by Zhang and Lister,[25] with $h_{\min} = 0.913\,(\tau/Oh)^{1/5}$, prevails for $Oh \gtrsim 1$ and $h_{\min}(\tau) \gg 1$, provided that the initial thickness $h_o \gtrsim 30$. The non-slender viscous regime reported by Moreno-Boza *et al.*,[19] where $h_{\min} = 0.665\,(\tau/Oh)^{1/3}$, applies for $Oh \gtrsim 1$ and $h_{\min}(\tau) \lesssim 4$, independently of the value of h_o. The slender inertial regime described by Garg *et al.*[10] for shear-thinning fluids has been shown to apply also for Newtonian fluids, but only for $Oh \lesssim 1$, $h_o \gtrsim 30$, and $h_{\min}(\tau) \gg 1$. The latter regime, where $h_{\min} = 1.0\,\tau^{2/7}$, experiences a crossover to the inertial regime discovered in the present work, which prevails for $Oh \lesssim 1$ and $h_{\min}(\tau) \lesssim 4$ for any value of h_o.

TABLE II. Physical properties, molecular Ohnesorge number, Oh, and global Ohnesorge number $Oh_o = \mu/\sqrt{\rho\sigma h_o^*} = Oh/\sqrt{h_o}$ for different liquid metals at their melting temperature, T_m, and at a higher working temperature, T_w. A value of $h_o^* = 40$ nm has been used to compute Oh_o.

Metal	T_w–T_m (K)	a (nm)	μ (mPa)	ρ (kg m^{-3})	σ (N m^{-1})	Oh	Oh_o
Cu	2000–1356	0.338–0.277	1.88–4.00	7400–8020	1.20–1.78	1.09–2.01	0.1–0.167
Ag	2000–1234	0.571–0.522	1.72–5.00	8671–9346	0.78–0.93	0.88–2.35	0.105–0.268
Ni	2000–1728	0.350–0.343	3.40–4.90	6700–7810	1.65–1.71	1.73–2.29	0.162–0.212
Rb	950–312	0.913–0.775	0.18–0.67	1460	0.064–0.088	0.62–2.12	0.094–0.295
Cs	930–302	1.138–0.965	0.19–0.68	1443–1843	0.041–0.057	0.73–2.13	0.123–0.33
Si	2000–1685	0.275–0.258	0.3–0.8	2500–2570	0.7–0.8	0.43–1.09	0.036–0.088

Let us finally point out that, in contrast with polymer films, for which $Oh \gg 1$, ultrathin liquefied metal films have associated values of $Oh \lesssim 1$, as recently pointed out by Kondic *et al.*[15] In such cases, the inertial regimes described in the present work may well be of practical relevance for the emergent field of liquid metal manipulation at sub-micrometer scales. Indeed, although the spinodal dewetting of liquefied metal films has received less attention than the corresponding regime in polymer films, there are a few experimental studies dealing with their instability, dynamics, and control[15] (see also references therein). Table II shows the physical properties and the molecular and global Ohnesorge numbers, Oh and Oh_o, respectively, of different liquid metals at their melting temperature, T_m, and at a higher working temperature, T_w. The experimental values of A, σ, ρ, and μ are obtained from the works of Battezzati and Greer,[2] Krishna *et al.*,[16] McKeown *et al.*,[18] and González *et al.*,[11] and in particular, the values of viscosity at T_w are obtained from Andrade's formula.[2] It is also important to note that there are still considerable uncertainties in the measurement of the associated Hamaker constant.[11,12,15] Note that the so-called molecular Ohnesorge number only depends on material quantities, and it does not involve any length as the global Ohnesorge number reported in Ref. 15. As a final but important note, it is deduced from the results of Table II and Fig. 1 that, for liquid metals at typical working temperatures, no self-similar regime is expected to be reached during film thinning. Indeed, for values of $Oh \gtrsim 0.4$, Fig. 1(d) reveals that the thinning dynamics of liquefied metals always takes place in transient regimes intermediate between the different regimes of Table I, except for the non-slender regime IV. However, as demonstrated in the present work, the latter regime is fully established below the molecular length scales.

ACKNOWLEDGMENTS

This paper is devoted to the memory of our beloved friend, Professor J. Fernández-Sáez (Pepe). His deep knowledge of mechanics and his enthusiasm and kindness have marked the lives and careers of countless students and colleagues. Key numerical advice of Dr. J. Rivero-Rodríguez is gratefully acknowledged. This research was funded by the Spanish MINECO, Subdirección General de Gestión de Ayudas a la Investigación, through Project No. RED2018-102829-T and by the Spanish MCIU-Agencia Estatal de Investigación through Project No. DPI2017-88201-C3-3-R, partly financed through FEDER European funds. A.M.-C. also acknowledges support from the Spanish MECD through the Grant No. FPU16/02562.

APPENDIX A: DISPERSION RELATION AND CHARACTERISTIC RUPTURE TIME

The linear modal dynamics of the film for $\varepsilon \ll 1$ are deduced by introducing the decomposition $\boldsymbol{\psi} = \boldsymbol{\psi}_0 + \varepsilon\hat{\boldsymbol{\psi}}\exp(ikx + \omega t)$, where $\boldsymbol{\psi}$ is a vector whose entries are the flow variables, $\boldsymbol{\psi}_0$ represents the unperturbed steady state, $\hat{\boldsymbol{\psi}}$ is a vector of complex amplitudes, k is the disturbance wavenumber, and ω is the disturbance growth rate. Standard manipulations[12,14] lead to a dispersion relation, which, in our variables, reads

$$\begin{aligned} &k\left(k^2 - 3h_o^{-4}\right)\left[\cosh(h_o\tilde{k})\sinh(h_o k) - \frac{k}{\tilde{k}}\cosh(h_o k)\sinh(h_o\tilde{k})\right] \\ &\quad + \left[\omega^2 + 4Oh^2k^2(k^2+\tilde{k}^2)\right]\cosh(h_o k)\cosh(h_o\tilde{k}) \\ &\quad - k\left[4Oh^2k(k^2+\tilde{k}^2) + (\omega^2 + 8Oh^2k^2\tilde{k}^2)\right. \\ &\quad \left.\times\ \frac{\sinh(h_o k)\sinh(h_o\tilde{k})}{\tilde{k}}\right] = 0, \end{aligned} \tag{A1}$$

where $\tilde{k}^2 = k^2 + \omega/Oh$. Figure 4 shows the rupture time, t_R, obtained from (A1) as a function of h_o for different values of Oh_l indicated in the legend. As briefly explained in Sec. II, this Ohnesorge number corresponds with the appropriate scales when studying the linear regime, namely, $\ell_c = h_o^*$, $p_c = A/(6\pi h_o^{*3})$, and $v_c = \sqrt{A/(6\pi\rho h_o^{*3})}$, where v_c can be obtained by balancing the inertial terms with the disjoining pressure gradient, $\rho\boldsymbol{v}\cdot\nabla\boldsymbol{v} \sim \nabla\phi$. Hence, this Ohnesorge number is deduced from the ratio between viscous and inertial terms, $Oh_l = \mu/(\rho v_c\ell_c) = Oh\sqrt{h_o}$.

The 7/2 exponent that is slightly observed when the Ohnesorge number takes the smallest realistic values can be deduced in the limit $Oh \ll 1$ of Eq. (A1), which reduces to $\omega^2 = \left(3h_o^{-4} - k^2\right)k\tanh(kh_o)$. This inviscid growth rate has the following small-k expansion:

$$\begin{aligned} \omega = k/\left(120\sqrt{3}h_o^{3/2}\right)&\left[360 - 60k^2h_o^2\left(1+h_o^2\right)\right. \\ &\left. + h_o^4\left(19 + 10h_o^2 - 5h_o^4\right)k^4\right] + O\left(k^7\right), \end{aligned} \tag{A2}$$

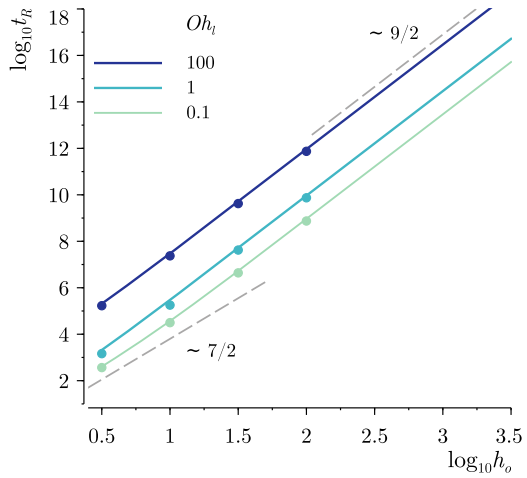

FIG. 4. Rupture time, t_R, as a function of h_o for different values of Oh_l indicated in the legend. Symbols correspond to the time extracted from the numerical simulations, and the lines are the linear prediction.

leading to an estimated non-dimensional rupture time

$$t_{\mathrm{R}} = \frac{(3+\sqrt{19})^{5/2}}{24(5+\sqrt{19})} h_o^{7/2} \ln(\varepsilon^{-1}) + O(h_o^{3/2}), \tag{A3}$$

defined by $t_{\mathrm{R}} = \ln(\varepsilon^{-1})/\omega_m$, where ω_m is the maximum growth rate, obtained by applying the condition $\partial\omega/\partial k = 0$. Equation (A3) reveals a strong dependence of the rupture time on the initial film thickness, $t_{\mathrm{R}} \propto h_o^{7/2}$. Conversely, when $Oh \gg 1$, the result for the rupture time obtained in Ref. 19 reads in inertial scales, $t_{\mathrm{R}} = 4/3 Oh\, h_o^{9/2}$.

The results of Garg *et al.*[10] are obtained by taking the value of the Weber number as $We = 7.37 \times 10^{-7}$ and thus $h_o = 1164.84$. The experimental values of the physical parameters of the film considered therein are $A = 10^{-9}$ J, $\sigma = 0.05$ Nm^{-1}, and $\mu = 35.6$ Pa s in the Newtonian case. The latter values yield $a = 0.326$ nm, and thus, the initial height of the film considered in Ref. 10 is $h_o^* = 379.43$ nm. It is important to note that the latter values of h_o and h_o^* are unrealistically large, and the vdW forces may not even trigger the instability. The values of the molecular and global Ohnesorge numbers are $Oh = 8.88 \times 10^6$ and $Oh_o = 7.62 \times 10^3$. Hence, the rupture time can be estimated by the Stokes limit reported in Refs. 19 and 23, which in dimensional form reads $t_{\mathrm{R}}^* = (4/3)(\mu a/\sigma)(h_o^*/a)^5$. Taking the latter values, one deduces the unrealistically large value of $t_{\mathrm{R}}^* = 6.63 \times 10^8$ s $\simeq 21$ years.

APPENDIX B: DIMENSIONAL ANALYSIS

The velocity components, (u^*, v^*), and the pressure, p^*, depend on the set of variables $(x^*, y^*, \tau_*, \rho, \mu, A, \sigma, h_o^*)$, while the film thickness h^* depends on the same variables except for y^*. Taking (τ_*, ρ, A) as the dimensional basis, the Buckingham Π theorem yields the reduced functional forms

$$\left[u^*, v^*\right] = \tau_*^{-3/5}(A/\rho)^{1/5}[\Pi_u, \Pi_v](\Pi_x, \Pi_y, \Pi_\sigma, \Pi_\mu, \Pi_{h_o}), \tag{B1a}$$

$$p^* = \tau_*^{-6/5}\left(A^2\rho^3\right)^{1/5}\Pi_p(\Pi_x, \Pi_y, \Pi_\sigma, \Pi_\mu, \Pi_{h_o}), \tag{B1b}$$

$$h^* = \tau_*^{2/5}(A/\rho)^{1/5}\Pi_h(\Pi_x, \Pi_\sigma, \Pi_\mu, \Pi_{h_o}), \tag{B1c}$$

where $[\Pi_x, \Pi_y, \Pi_{h_o}] = \tau_*^{-2/5}(\rho/A)^{1/5}[x^*, y^*, h_o^*]$, $\Pi_\sigma = \tau_*^{4/5}\sigma/(\rho^{2/5}A^{3/5})$, and $\Pi_\mu = \tau_*^{1/5}\mu/(\rho^{3/5}A^{2/5})$. Note that Π_μ^{-1} and Π_σ^{-1} can be interpreted as the local Reynolds and Weber numbers, respectively (see Sec. III). In the limit $\tau_* \to 0$, $\Pi_\mu \to 0$, $\Pi_\sigma \to 0$, and $\Pi_{h_o} \to \infty$, indicating that as rupture is approached, viscous and surface tension forces become negligible and that the flow becomes independent of h_o, thereby suggesting the existence of a similarity solution of the first kind for $\tau \to 0$, with liquid inertia balancing vdW forces. In addition, the fact that x^* and y^* have the same asymptotic scaling indicates that the near-rupture local flow is non-slender and that lubrication theory, which assumes that the characteristic length in the x direction is much larger than the film thickness, necessarily fails to describe the singularity.

APPENDIX C: NUMERICAL TECHNIQUES

We describe the numerical techniques employed to solve the Navier–Stokes equations (3)–(4b), the self-similar potential problem (23)–(24b), and the boundary-layer problems (28a), (28b), and (29). Most of the equations were written in a weak form upon convenient use of Green's identities, rendering them amenable for the use of finite elements for the spatial discretization. The implementation was carried out in the finite-element solver COMSOL MULTIPHYSICS.

1. Navier–Stokes equations

The Navier–Stokes equations of motion and corresponding boundary conditions (3) and (4b) were first written in a weak form with the use of suitable test functions for velocity and pressure, i.e., $\tilde{\boldsymbol{v}}$ and $\tilde{p}$, yielding the bilinear form

$$0 = \int_{\mathcal{V}}\left[\frac{\mathrm{D}\boldsymbol{v}}{\mathrm{D}t}\cdot\tilde{\boldsymbol{v}} - p\nabla\cdot\tilde{\boldsymbol{v}} + Oh\left(\nabla\boldsymbol{v} + \nabla\boldsymbol{v}^{\mathrm{T}}\right):\nabla\tilde{\boldsymbol{v}} + \tilde{p}\nabla\cdot\boldsymbol{v}\right]\mathrm{d}\mathcal{V} + \int_{\Sigma_s}\left(\nabla_s\cdot\tilde{\boldsymbol{v}} + h^{-3}\boldsymbol{n}\cdot\tilde{\boldsymbol{v}}\right)\mathrm{d}\Sigma, \tag{C1}$$

where the surface gradient operator is defined as $\nabla_s = (\mathsf{I} - \boldsymbol{nn})\cdot\nabla$, with I being the identity tensor, and $\boldsymbol{n}$ is the outward-pointing normal unit vector. Note that the disjoining pressure term has been conveniently rewritten as a surface force after judicious application of Gauss's theorem. A schematic of the numerical domain and boundary conditions is presented in Fig. 5. Equation (C1) was discretized using Taylor–Hood triangular elements for pressure and velocity (also the corresponding test functions) to ensure numerical stability. The use of an arbitrary Lagrangian–Eulerian (ALE) technique for the tracking of the interface allowed us to impose the kinematic boundary condition (4a) along Σ_s by prescribing the normal velocity of the mesh to that of the fluid. The displacement of the mesh

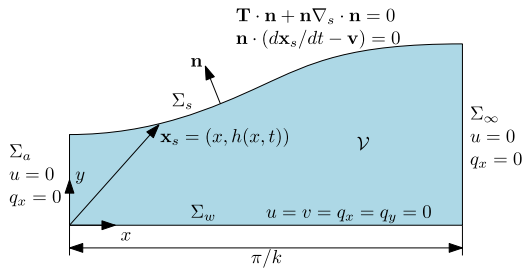

FIG. 5. Sketch of the numerical domain $\mathcal{V}$ bounded by Σ_a (symmetry axis at $x = 0$), Σ_w (bottom wall), Σ_∞ (symmetry axis at $x = \pi/k$), and Σ_s (free surface). The corresponding boundary conditions for the velocity, stresses, and mesh displacement are also included in the schematic.

elements was computed by solving a Laplace equation for the displacement field $\boldsymbol{q} = (q_x, q_y)$, namely $\nabla^2\boldsymbol{q} = 0$, with suitable boundary conditions. The entire system is advanced in time using a variable-order BDF technique with an adaptive time step until numerical rupture.

2. Potential flow

The elliptic system comprised of the Laplace Eq. (23) and the boundary conditions (24a) and (24b) were again written in a weak form, producing

$$\int_{\mathcal{V}} \nabla\Phi\cdot\nabla\tilde{\Phi}\,\mathrm{d}\mathcal{V} = 0, \tag{C2}$$

which is complemented with the boundary condition $\Phi = \Phi_s$ at Σ_s, where Φ_s is the yet-unknown value of the potential at the free surface, leveraged as a Lagrange multiplier to solve the boundary PDE

$$\int_{\Sigma_s}\left[\frac{1}{f^3}+\frac{1}{5}\Phi+\frac{2}{5}(\xi\Phi_\xi+\eta\Phi_\eta)+\frac{1}{2}\left(\Phi_\xi^2+\Phi_\eta^2\right)\right]\tilde{\Phi}_s\,\mathrm{d}\Sigma = 0, \tag{C3}$$

where $\tilde{\Phi}_s$ is the test function for the potential at the free surface, which effectively enforces the Euler–Bernoulli condition at the interface. The ALE method was once again used for the displacement of the mesh. This allowed us to achieve the kinematic condition (24b) by introducing an extra degree of freedom for the vertical displacement of the deformable mesh δ at Σ_s. The boundary condition for the displacement of the free surface then becomes $\boldsymbol{q} = \delta\boldsymbol{e}_y$ at Σ_s, and the corresponding restriction for δ may be viewed as a surface PDE of the form

$$\int_{\Sigma_s}\left[\frac{2}{5}f+\Phi_\eta-f_\xi\left(\frac{2}{5}\xi+\Phi_\xi\right)\right]\tilde{\delta}\,\mathrm{d}\Sigma = 0, \tag{C4}$$

where $\tilde{\delta}$ is the test function for the vertical displacement δ discretized using first-order Lagrange elements and $\mathrm{d}\Sigma$ is the line element along Σ_s. This additional equation enabled us to use a standard Newton–Raphson root-finding algorithm to iteratively solve all the unknowns upon a normalized tolerance, fixed to 10^{-6}, provided a suitable initial guess. A summary of the procedure is sketched in Fig. 6.

3. Boundary layer equations

Equations (28a) and (28b) were treated using ξ as a temporal variable, thereby making the system parabolic. Finite elements were employed across the transversal direction ζ upon writing the corresponding weak form, namely,

$$\int_0^{\zeta_\infty}\left\{\left(\tilde{U}_\xi+\tilde{V}_\zeta\right)\bar{V}+\left[\frac{3}{5}\tilde{U}+\left(\frac{2\xi}{5}+\tilde{U}\right)\tilde{U}_\xi+\left(\frac{\zeta}{2}+\tilde{V}\right)+P_\xi\right]\bar{U}+\tilde{U}_\zeta\bar{U}_\zeta\right\}\mathrm{d}\zeta = 0, \tag{C5}$$

where $\bar{U}$ and $\bar{V}$ are quadratic test functions for the variables $\tilde{U}$ and $\tilde{V}$, respectively, P_ξ is the known external pressure gradient whose expression is given in the main text, and $\zeta_\infty \simeq 60$ is the numerical infinity. The system was integrated with the boundary conditions $\tilde{U} = \tilde{V} = 0$ at $\zeta = 0$ and marched in time using a BDF algorithm provided the *initial condition* for $\xi \ll 1$. Such a condition was obtained by solving the problem (29) in terms of the local stream function $\xi G(\zeta)$ using a pseudospectral collocation technique,[9] as described in the main text.

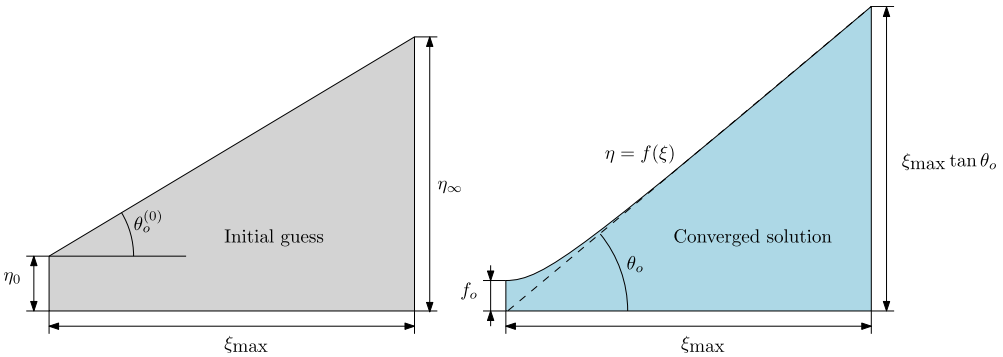

FIG. 6. Sketch of the initial guess (left-hand side panel) for the computation of the self-similar film shape and final converged solution (right-hand side panel). Note that in particular, $f(\xi)$ and θ_o are obtained as part of the solution.

DATA AVAILABILITY

The data that support the findings of this study are available from the corresponding author upon reasonable request.

REFERENCES

[1]A. Alizadeh Pahlavan, L. Cueto-Felgueroso, A. E. Hosoi, G. H. McKinley, and R. Juanes, "Thin films in partial wetting: Stability, dewetting and coarsening," J. Fluid Mech. **845**, 642–681 (2018).

[2]L. Battezzati and A. L. Greer, "The viscosity of liquid metals and alloys," Acta Metall. **37**(7), 1791–1802 (1989).

[3]R. Blossey. *Thin Liquid Films: Dewetting and Polymer Flow* (Springer Science & Business Media, 2012).

[4]D. Bonn, J. Eggers, J. Indekeu, J. Meunier, and E. Rolley, "Wetting and spreading," Rev. Mod. Phys. **81**(2), 739 (2009).

[5]R. V. Craster and O. K. Matar, "Dynamics and stability of thin liquid films," Rev. Mod. Phys. **81**(3), 1131 (2009).

[6]P. G. De Gennes, "Wetting: Statics and dynamics," Rev. Mod. Phys. **57**(3), 827 (1985).

[7]T. DebRoy, H. L. Wei, J. S. Zuback, T. Mukherjee, J. W. Elmer, J. O. Milewski, A. M. Beese, A. Wilson-Heid, A. De, and W. Zhang, "Additive manufacturing of metallic components–process, structure and properties," Prog. Mater. Sci. **92**, 112–224 (2018).

[8]M. D. Dickey, "Emerging applications of liquid metals featuring surface oxides," ACS Appl. Mater. Interfaces **6**(21), 18369–18379 (2014).

[9]T. A. Driscoll, N. Hale, and L. N. Trefethen, Chebfun guide, 2014.

[10]V. Garg, P. M. Kamat, C. R. Anthony, S. S. Thete, and O. A. Basaran, "Self-similar rupture of thin films of power-law fluids on a substrate," J. Fluid Mech. **826**, 455–483 (2017).

[11]A. G. González, J. A. Diez, Y. Wu, J. D. Fowlkes, P. D. Rack, and L. Kondic, "Instability of liquid Cu films on a SiO_2 substrate," Langmuir **29**(30), 9378–9387 (2013).

[12]A. G. González, J. A. Diez, and M. Sellier, "Inertial and dimensional effects on the instability of a thin film," J. Fluid Mech. **787**, 449–473 (2016).

[13]H. C. Hamaker, "The London-van der Waals attraction between spherical particles," Physica **4**(10), 1058–1072 (1937).

[14]K. Kargupta, A. Sharma, and R. Khanna, "Instability, dynamics, and morphology of thin slipping films," Langmuir **20**(1), 244–253 (2004).

[15]L. Kondic, A. G. González, J. A. Diez, J. D. Fowlkes, and P. Rack, "Liquid-state dewetting of pulsed-laser-heated nanoscale metal films and other geometries," Annu. Rev. Fluid Mech. **52**, 235–262 (2019).

[16]H. Krishna, N. Shirato, C. Favazza, and R. Kalyanaraman, "Energy driven self-organization in nanoscale metallic liquid films," Phys. Chem. Chem. Phys. **11**(37), 8136–8143 (2009).

[17]T. Lundgren and P. Koumoutsakos, "On the generation of vorticity at a free surface," J. Fluid Mech. **382**, 351–366 (1999).

[18]J. T. McKeown, N. A. Roberts, J. D. Fowlkes, Y. Wu, T. LaGrange, B. W. Reed, G. H. Campbell, and P. D. Rack, "Real-time observation of nanosecond liquid-phase assembly of nickel nanoparticles via pulsed-laser heating," Langmuir **28**(49), 17168–17175 (2012).

[19]D. Moreno-Boza, A. Martínez-Calvo, and A. Sevilla, "Stokes theory of thin-film rupture," Phys. Rev. Fluids **5**(1), 014002 (2020).

[20]A. Oron, S. H. Davis, and S. G. Bankoff, "Long-scale evolution of thin liquid films," Rev. Mod. Phys. **69**(3), 931 (1997).

[21]L. Rosenhead, *Laminar Boundary Layers* (Clarendon Press, Oxford, 1963).

[22]E. Ruckenstein and R. K. Jain, "Spontaneous rupture of thin liquid films," J. Chem. Soc., Faraday Trans. 2 **70**, 132–147 (1974).

[23]A. Vrij, "Possible mechanism for the spontaneous rupture of thin, free liquid films," Discuss. Faraday Soc. **42**, 23–33 (1966).

[24]B. W. Zeff, B. Kleber, J. Fineberg, and D. P. Lathrop, "Singularity dynamics in curvature collapse and jet eruption on a fluid surface," Nature **403**(6768), 401 (2000).

[25]W. W. Zhang and J. R. Lister, "Similarity solutions for van der Waals rupture of a thin film on a solid substrate," Phys. Fluids **11**(9), 2454–2462 (1999).